In-plane uniaxial stress effects on the structural and electronic properties of BaFe$_2$As$_2$ and CaFe$_2$As$_2$

Milan Tomić,[1] Harald O. Jeschke,[1] Rafael M. Fernandes,[2] and Roser Valentí[1]

[1]*Institut für Theoretische Physik, Goethe-Universität Frankfurt, Max-von-Laue-Straße 1, 60438 Frankfurt am Main, Germany*

[2]*School of Physics and Astronomy, University of Minnesota, Minneapolis, Minnesota 55455, USA*

Starting from the orthorhombic magnetically ordered phase, we investigate the effects of uniaxial tensile and compressive stresses along **a**, **b**, and the diagonal **a** + **b** directions in BaFe$_2$As$_2$ and CaFe$_2$As$_2$ in the framework of *ab initio* density functional theory (DFT) and a phenomonological Ginzburg-Landau model. While—contrary to the application of hydrostatic or *c*-axis uniaxial pressure—both systems remain in the orthorhombic phase with a pressure-dependent nonzero magnetic moment, we observe a sign-changing jump in the orthorhombicity at a critical uniaxial pressure, accompanied by a reversal of the orbital occupancy and a switch between the ferromagnetic and antiferromagnetic directions. Our Ginzburg-Landau analysis reveals that this behavior is a direct consequence of the competition between the intrinsic magneto-elastic coupling of the system and the applied compressive stress, which helps the system to overcome the energy barrier between the two possible magneto-elastic ground states. Our results shed light on the mechanisms involved in the detwinning process of an orthorhombic iron-pnictide crystal and on the changes in the magnetic properties of a system under uniaxial stress.

I. INTRODUCTION

Since the discovery of high-T_c superconductivity in Fe-based materials in 2008,[1] an enormous amount of effort has been invested to understand the microscopic behavior of these systems. Iron pnictides and chalcogenides become superconductors either by hole or electron doping the systems, by application of external pressure or by a combination of both. In particular, uniaxial pressure is currently being intensively discussed as a possible route towards modifying the structural, magnetic, and even superconducting properties of these systems. A regular sample below its magnetic and structural transition temperatures displays an equal number of opposite twin orthorhombic domains, effectively canceling out its anisotropic properties. To circumvent this issue and obtain a single orthorhombic domain sample, uniaxial tensile stress has been widely employed to detwin iron pnictides such as BaFe$_2$As$_2$ and CaFe$_2$As$_2$[2–8] and unveil their anisotropic properties, which have been argued to originate from electronic nematic degrees of freedom.[9–11] Theoretically, although it is clear that in the tetragonal phase the applied uniaxial pressure acts as a conjugate field to the orthorhombic order parameter, condensing a single domain,[12] the nature of the detwinning process deep inside the orthorhombic phase remains an open question, since different mechanisms might be at play, such as twin boundary motion or reversal of the order parameter inside the domains.[8,13]

Besides promoting detwinning, uniaxial strain has also been shown to affect the thermodynamic properties of the iron pnictides. Recent neutron scattering experiments on BaFe$_2$As$_2$ under compressive stress along the in-plane **b** direction reported a progressive shift to higher temperatures of the magnetic transition[6]—a behavior also seen in BaFe$_2$(As$_{1−x}$P$_x$)$_2$ by thermodynamic measurements[14]—and an apparent reduction of the magnetic moment.[6] Moreover, Blomberg *et al.* observed a significant uniaxial structural distortion in BaFe$_2$As$_2$ under tensile stress, suggesting an enhanced response to external strain.[7] More recently, it was found that epitaxially strained thin films of FeSe on a SrTiO$_3$ substrate show an increase in

critical superconducting temperatures up to 65 K, the highest reported T_c so far.[15] Clearly, crystal lattice strain plays a key role for the magnetic,[16] structural, and superconducting properties in Fe-based superconductors, and a better understanding of the microscopic origin of such behavior is desirable.

In this work we combine density functional theory (DFT) calculations and Ginzburg-Landau phenomenology to analyze the effects of uniaxial compressive stress as well as uniaxial tensile stress on the magnetic, electronic and structural properties of BaFe$_2$As$_2$ and CaFe$_2$As$_2$ at low temperatures, deep inside the ordered phase. Stress is measured in terms of equivalent hydrostatic pressure, $P = \text{Tr}(\hat{\sigma})/3$, where $\hat{\sigma}$ is the stress tensor matrix and positive and negative pressures correspond to applying compressive and tensile stresses respectively. Our *ab initio*-derived estimates for the elastic constants in the orthorhombic phase agree well with experimental values. While no sign of a true structural or magnetic phase transition is observed in the range of pressures between −2 and 2 GPa, at a critical pressure we observe a reversal of the magnetization, i.e., exchange of ferromagnetic (FM) and antiferromagnetic (AFM) directions, simultaneous to a discontinuous change in the orthorhombic order parameter $a − b$, which also changes sign. This behavior has important consequences on the orbital d_{xz} and d_{yz} occupancies and is also related to the shift of the magnetic ordering temperature, as we argue below.

Furthermore, by employing a phenomenological Ginzburg-Landau model, we show that this behavior is intimately connected to the magneto-elastic coupling of the system, which by itself acts as an intrinsic conjugate field to the orthorhombic order parameter. As the applied compressive stress is enhanced towards a critical value, it eventually overcomes the effects of the magneto-elastic coupling, rendering the zero-pressure state energetically unstable and resulting in a simultaneous reversal of the magnetization and the orthorhombic order parameter. Comparison of the DFT-derived critical uniaxial pressures for CaFe$_2$As$_2$ and BaFe$_2$As$_2$, combined with the Ginzburg-Landau result that the critical pressure is proportional to the magneto-elastic coupling, suggests that the latter

is larger in $CaFe_2As_2$ than in $BaFe_2As_2$. We also propose low-temperature detwinning measurements to compare the experimental critical pressure with our *ab initio* estimates in order to clarify the dominant mechanism behind the detwinning process of orthorhombic iron pnictide crystals.

The paper is organized as follows: in Sec. II we summarize our computational methods, and in Sec. III we present our DFT results. Section IV is devoted to the Ginzburg-Landau analysis and comparison with DFT calculations. Section V contains the discussions and concluding remarks. Details about the *ab initio* method are presented in the Appendix.

II. COMPUTATIONAL METHODS

Electronic structure calculations were performed within DFT with the Vienna Ab initio Simulations Package (VASP)[17] with the projector augmented wave (PAW) basis[18] in the generalized gradient approximation (GGA). All our structural relaxations were performed under constant stress using the Fast Inertial Relaxation Engine (FIRE).[19,20] For this purpose, we had to modify the algorithm accordingly (see Appendix). Every 10 steps, we cycled through nonmagnetic, ferromagnetic, antiferromagnetic-checkerboard, stripe-type antiferromagnetic (along unit cell axis **a**), and stripe-type antiferromagnetic (along unit cell axis **b**) spin configurations, and then we continued the relaxation with the lowest energy spin configuration. As a final converged magnetic configuration in the orthorhombic phase we always found stripe-type antiferromagnetic order either along **a** or along **b**, as discussed below.

The energy cutoff in the calculations was set to 300 eV and a Monkhorst-Pack uniform grid of $(6 \times 6 \times 6)$ points was used for the integration of the irreducible Brillouin zone (BZ).

III. RESULTS AND DISCUSSION

A. $BaFe_2As_2$

Starting from the low-temperature orthorhombic structure with stripe magnetic order, we performed structure relaxations under applied uniaxial tensile and compressive stresses along **a** (AFM direction), **b** (FM direction), and the plane-diagonal **a** + **b** direction for both $BaFe_2As_2$ and $CaFe_2As_2$ [see inset of Fig. 1(a)]. We measure stress in units of the equivalent hydrostatic pressure, $P = \text{Tr}(\hat{\sigma})/3$, with $\hat{\sigma}$ denoting the stress tensor matrix. We simulated pressures in the range between -3 and 3 GPa. In the tensile stress range, below -2.7 GPa we observe in both systems that, for stress along **a**, a sudden expansion in a and contraction in b and c axes occurs. A similar situation arises when pulling apart along **b**. This feature signals the extreme case of absence of bonding within the material, and for this reason this pressure range will be excluded from further discussion.

Figure 1 shows the evolution of lattice parameters for $BaFe_2As_2$ as a function of uniaxial stress along **a**, **b** and **a** + **b**. We consider both compressive stress (positive pressure) and tensile stress (negative pressure). At $P = 0$ GPa, we have a (AFM direction) $> b$ (FM direction). $BaFe_2As_2$ remains in the orthorhombic phase with nonzero increasing magnetic moment for large tensile stress (negative pressure). Pulling apart (i.e., $P < 0$) along the (longer) AFM direction **a** [Fig. 1(a)] the system expands along **a**, strongly compresses along **c**, and shows almost no changes along **b**; similarly, pulling apart along the (shorter) FM direction **b** [Fig. 1(b)] b expands, c compresses and a shows almost no changes except at the pressure $P = -0.22$ GPa [Fig. 1(e)]. At this point, $BaFe_2As_2$ shows a sudden jump in the orthorhombicity where **a** becomes the shorter axis and **b** becomes the longer
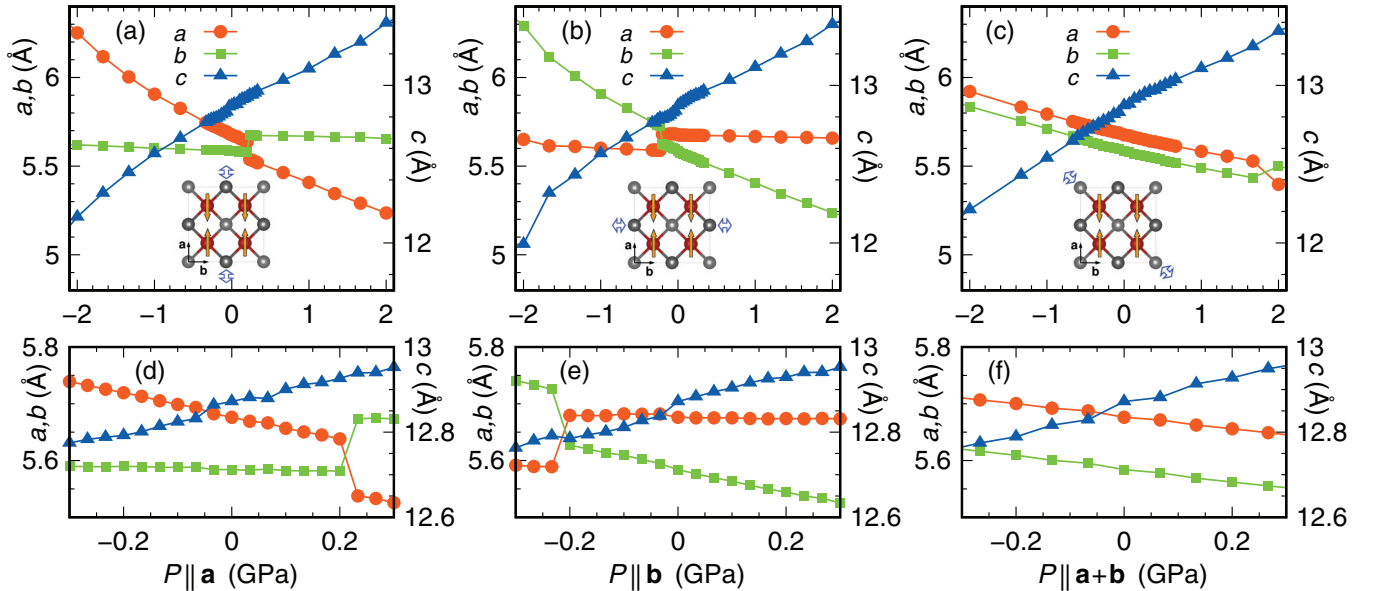

FIG. 1. (Color online) Evolution of the unit cell parameters in $BaFe_2As_2$ under application of uniaxial stress in the equivalent hydrostatic pressure range $[-2\,\text{GPa}, 2\,\text{GPa}]$ (a) along **a**, (b) along **b**, and (c) along **a** + **b**. Panels (d)–(f) show the corresponding zoom of the pressure dependence of the lattice parameters in the range $[-0.3\,\text{GPa}, 0.3\,\text{GPa}]$. Negative pressures correspond to tensile stress while positive pressures correspond to compressive stress. Note, that the relationship between axes and iron moments shown in the inset in (a) is valid for $P \parallel \mathbf{a} < 0.22$ GPa, and in (b) for $P \parallel \mathbf{b} > -0.22$ GPa. For a discussion of the reversal of AFM order, see the text.
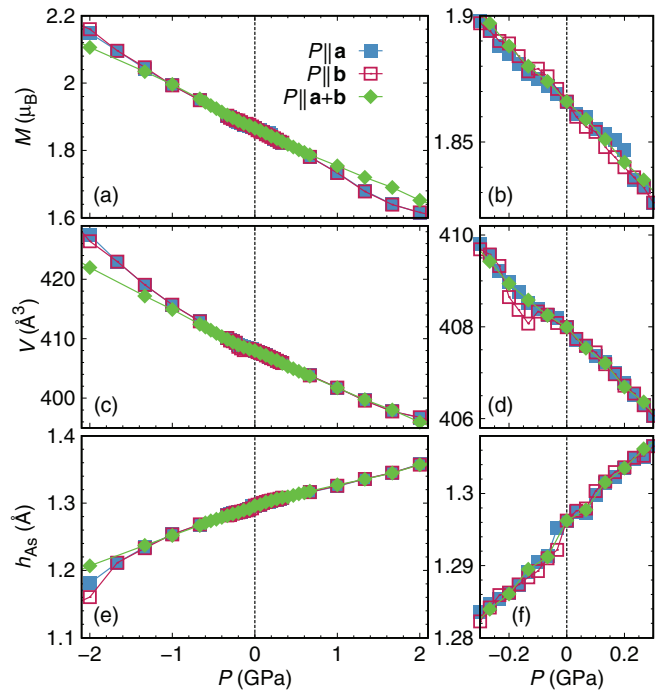
FIG. 2. (Color online) (a) Evolution of the magnetic moments of iron, (c) of the unit cell volume, and (e) of the pnictogen height under uniaxial pressure in the range $[-2\,\mathrm{GPa}, 2\,\mathrm{GPa}]$. Panels (b), (d), and (e) show the corresponding zoom of the pressure dependence of these quantities in the range $[-0.3\,\mathrm{GPa}, 0.3\,\mathrm{GPa}]$. Negative pressures correspond to tensile stress while positive pressures correspond to compressive stress.

axis. This interchange happens with a rotation of the magnetic order by 90 degrees, i.e., the FM direction becomes parallel to the **a** axis while the AFM direction becomes parallel to the **b** axis. We will discuss this feature further below. Note that tensile stress along **a** + **b** acts similarly on both **a** and **b** directions, which expand, while the **c** direction strongly compresses [Figs. 1(c) and 1(f)].

Under application of compressive stress (positive pressure), we observe in all three cases a strong expansion along **c** and a compression along the direction of applied stress (**a**, **b**, or **a** + **b**). For the cases where pressure is applied along **a** or **b**, we observe almost no changes or a slight expansion along **b** and **a**, respectively. Since $a > b$ at zero stress, we observe the inversion of axes followed by a jump in orthorhombicity and a 90 degree rotation of the magnetization when stress is applied along **a** at $P = 0.22$ GPa [Figs. 1(a) and 1(d)]. This inversion of axes, with $b > a$ for all higher compressive stress values means that the spin configuration shown in the inset of Fig. 1(a) should now be turned by 90 degrees, with **b** pointing along the AFM direction. Such an inversion is also observed for compressive stress along **a** + **b** at much larger pressures of $P = 2$ GPa.

Figure 2 shows the evolution of magnetic moment, volume and As height in $BaFe_2As_2$ as a function of stress. The three quantities show a clearly monotonic behavior independent of the applied stress direction except for small jumps at the pressures $P = -0.22$ GPa (for stress along **a**) and $P = 0.22$ GPa (for stress

along **b**) where the tetragonal condition is almost fulfilled ($a \approx b$) [Figs. 2(b), 2(d), and 2(f)]. We also note here how magnetic moments in $BaFe_2As_2$ respond to different direction of pressure application. The highest rate of suppression, of roughly $0.1\mu_B/$GPa is achieved when pressure is applied within the ab plane, while application of pressure along the **c** axis actually results in magnetic moment increase by $0.03\mu_B/$GPa.[20] Even though DFT calculations overestimate the value of the ordered Fe magnetic moment at $P = 0$ GPa, it is to be expected that the relative changes in magnetic moment should provide a reliable description of the situation of $BaFe_2As_2$ under pressure as shown in previous studies.[20–23]

Except for the pressures $P = -0.22$ GPa (for stress along **a**) and $P = 0.22$ GPa (for stress along **b**), stress always enforces a certain degree of orthorhombicity and the system remains magnetically ordered with a decreasing ordered moment as a function of compressive stress [Fig. 2(a)]. Moreover, since the c axis continually expands from negative to positive pressures, h_{As} increases accordingly as a function of stress [Fig. 2(e)]. These features have a direct consequence on the electronic properties of the system.

As an illustration, we show in Fig. 3 the (nonspin polarized) Fermi surface of $BaFe_2As_2$ under application of uniaxial stress $P = -0.07$ GPa and $P = 1.7$ GPa applied along **a** in the 1 Fe/unit cell equivalent Brillouin zone. We would like to note that correlation effects beyond DFT as implemented in DFT + DMFT (dynamical mean field theory), which are known to give a good agreement between the calculated Fermi surfaces and angle-resolved photoemission measurements in the Fe pnictides,[24–29] have not been included here. Modest tensile stress of 0.07 GPa leads to the disappearance of the $3d_{xy}$ hole pocket around $\bar{\Gamma}$ in the $k_z = 0$ plane [see Fig. 5(a) in Ref. 20]. On the other hand, when compressive stress is applied, the hole pockets around $\bar{\Gamma}$ significantly change in size, and additionally at a pressure of 1.7 GPa, small electron pockets, of majority $3d_{xy}$ and $3d_{z^2}$ character, appear along the $\bar{\Gamma}$-$\bar{M}$ directions of the BZ [Figs. 3(c) and 3(e)]. The increase of the $3d_{xy}$ hole pocket size with increasing uniaxial stress can be explained by the reduction of Fe-Fe distances along the **a** axis, leading to an increased contribution of $3d_{xy}$-$3d_{xy}$ bonding. In fact, the effects of tensile and compressive stress on the electronic structure shown for the example of stress along **a** can be seen also in our calculations for both stress along **b** and along **a** + **b**.

In Fig. 4 we analyze the orbitally-resolved density of states at the Fermi level $N(E_F)$. Applying stress both along **a** and **b** has the same effect on the total density of states of both $BaFe_2As_2$ and $CaFe_2As_2$, but there is a selective orbital order as shown in Fig. 4. $N(E_F)$ is predominantly of $3d_{xz}$ character when $a > b$ and of $3d_{yz}$ character when $a < b$. This means that the dominant character switches from $3d_{yz}$ to $3d_{xz}$ at $P \parallel$ **a** ≈ 0.22 GPa, and from $3d_{xz}$ to $3d_{yz}$ at $P \parallel$ **b** ≈ -0.22 GPa as expected.

B. $CaFe_2As_2$

The lattice parameters of $CaFe_2As_2$ under application of compressive stress along **a**, **b** and **a** + **b** directions show a similar overall behavior compared to $BaFe_2As_2$ (see Fig. 5)
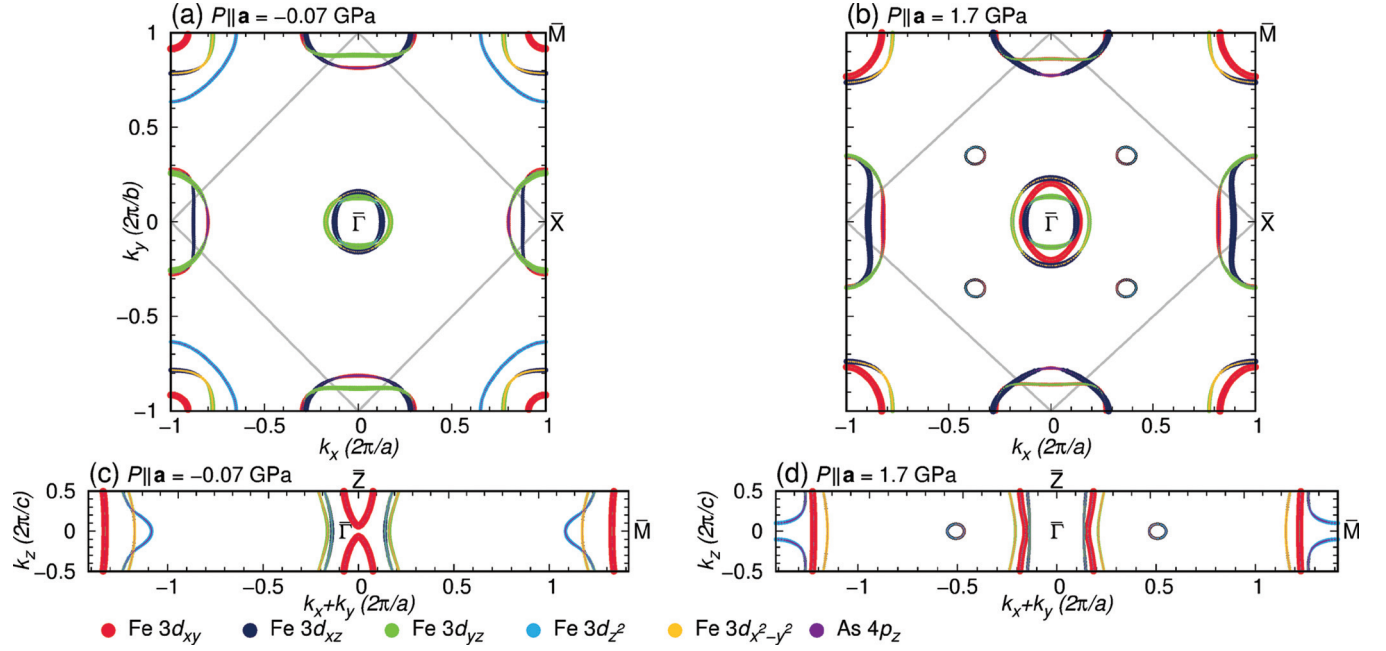
FIG. 3. (Color online) Fermi surface of BaFe$_2$As$_2$ for two pressure values of uniaxial stress applied along the **a** axis shown in the 1 Fe/unit cell equivalent BZ (see Ref. 34 for the BZ path definition). Panels (a) and (b) show $k_z = 0$ cuts of the Fermi surface at pressures of -0.07 and 1.7 GPa respectively, while panels (c) and (d) show vertical cuts along the diagonal of the BZ for pressures of -0.07 and 1.7 GPa. Grey lines on panels (a) and (b) denote boundaries of the 2 Fe/unit cell BZ.

except for some important shifts of the pressures at which the system exchanges the FM and AFM directions. When stress is applied along the **a** direction, we observe at $P =$
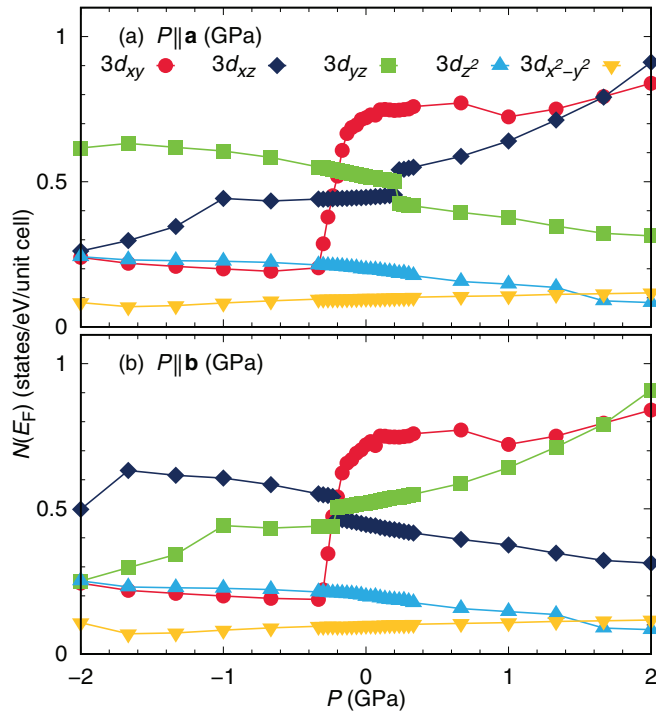

FIG. 4. (Color online) Evolution of the orbital resolved density of states of BaFe$_2$As$_2$ at the Fermi level $N(E_F)$ with stress (a) applied along **a**, and (b) along **b**. Lines joining the calculated points are a guide for the eye.

0.67 GPa a jump in the orthorhombic order parameter, with a sign change, accompanied by a reversal of the magnetic AFM and FM directions. However, analogously to the case of BaFe$_2$As$_2$, this is not followed by a suppression of the magnetic moments of iron. In fact, the c axis expands with applied stress and at $P = 0.67$ GPa the c lattice parameter in CaFe$_2$As$_2$ is too large for the formation of an interlayer As-As covalent bond, necessary for a transition to a collapsed tetragonal phase and suppression of magnetic moments as observed under hydrostatic or c-axis uniaxial pressure.[20–22,30] For tensile stress along the (shorter) **b** direction, the reversal of AFM and FM directions happens at $P = -0.33$ GPa followed by a jump in the orthorhombicity. The magnetic response of CaFe$_2$As$_2$ is highly anisotropic as well, but contrary to the case of BaFe$_2$As$_2$, the magnetic moments in CaFe$_2$As$_2$ are most effectively suppressed when pressure is applied along **c**. We measure a rate of about $0.1\mu_B$/GPa.[20] Application of pressure within the ab plane results in a suppression of the magnetic moment at a rate of $0.02\mu_B$/GPa.

In order to investigate the possibility of a structural and/or magnetic phase transition at higher pressures, we concentrate now on compressive stress along the diagonal of the ab plane. We find that orthorhombicity is preserved up to 7.7 GPa, where a sharp transition to a tetragonal phase appears. This transition is of first-order type, like the orthorhombic to collapsed tetragonal phase transition under application of hydrostatic or uniaxial pressure along the **c** axis[20] but in this case, changes of magnetic and structural properties take opposite directions; the **c** axis undergoes a sudden expansion of about 9.5%, and **a** and **b** axes contract while the iron magnetic moments order ferromagnetically and sharply increase in value by around 25%. Interestingly though, contrary to the application of
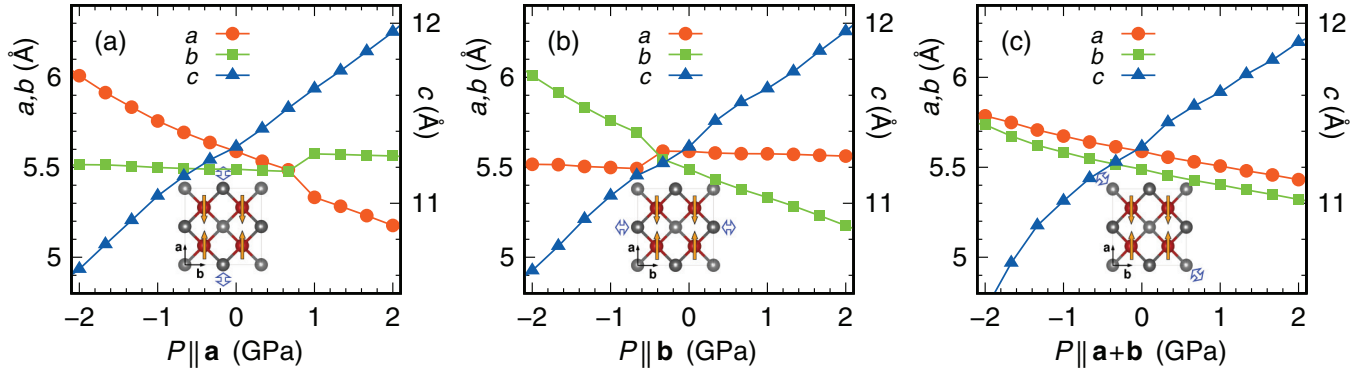
FIG. 5. (Color online) Evolution of the unit cell parameters in $CaFe_2As_2$ under the application of uniaxial stress in the range $[-2\,\mathrm{GPa}, 2\,\mathrm{GPa}]$ (a) along **a**, (b) along **b**, and (c) along **a** + **b**. Negative pressures correspond to tensile stress while positive pressures correspond to compressive stress. Note that the relationship between axes and iron moments shown in the inset in (a) is valid for $P||\mathbf{a} < 1$ GPa, and in (b) for $P||\mathbf{b} > -0.6$ GPa.

hydrostatic and uniaxial pressure along **c** axis, the volume change here is significantly smaller, namely an expansion by about 0.9%. These features are not observed in $BaFe_2As_2$ when we compress along the diagonal of the ab plane up to pressures of 10 GPa.

C. Elastic constants in the orthorhombic phase

Using data for the response to the uniaxial stress along **a**, **b**, and **c**[20] axes we can directly evaluate the elastic constants C_{ij} in $BaFe_2As_2$ and $CaFe_2As_2$ corresponding to the orthorhombic deformations. We define elastic constants to be such that

$$\sigma_i = \sum_j C_{ij} u_j,$$

where σ_i and u_j are stress and strain tensor components respectively, and indices i and j can be xx, yy, zz. Strains are defined to be $u_{xx} = (a - a_0)/a_0$, $u_{yy} = (b - b_0)/b_0$, and $u_{zz} = (c - c_0)/c_0$, where a_0, b_0, and c_0 are equilibrium unit cell dimensions ($P = 0$ GPa). We first directly obtain $S_{ij} = [C^{-1}]_{ij}$ by performing linear fits to $u_i(\sigma_j)$ and C is then obtained by inverting the resulting matrix. For $BaFe_2As_2$, the elastic constant matrix is

$$C = \begin{bmatrix} 95.2 \pm 4.3 & 20.4 \pm 3.4 & 40.8 \pm 4.5 \\ 27.3 \pm 4.8 & 130.8 \pm 6.1 & 64.0 \pm 7.0 \\ 43.7 \pm 4.5 & 47.7 \pm 4.6 & 81.0 \pm 5.6 \end{bmatrix} \text{ GPa}. \quad (1)$$

Utilizing Voigt and Reuss averages,[31] defined as

$$B_{\mathrm{Voigt}} = \tfrac{1}{9}[C_{11} + C_{22} + C_{33} + 2(C_{12} + C_{13} + C_{23})],$$

$$B_{\mathrm{Reuss}} = [S_{11} + S_{22} + S_{33} + 2(S_{12} + S_{13} + S_{13})]^{-1},$$

it is possible to estimate the bulk modulus. Voigt and Reuss averages yield 61.9 ± 5.1 and 69.3 ± 7.5 GPa, respectively, which is in good agreement with our previous estimate[20] and the experimental value of 59 ± 2 GPa.[32] For $CaFe_2As_2$, the elastic constant matrix is given by

$$C = \begin{bmatrix} 148.7 \pm 18.5 & 45.6 \pm 12.3 & 55.5 \pm 12.7 \\ 63.9 \pm 21.4 & 182.4 \pm 18.4 & 81.2 \pm 17.5 \\ 61.4 \pm 14.7 & 63.1 \pm 11.4 & 68.8 \pm 11.3 \end{bmatrix} \text{ GPa}, \quad (2)$$

which results in bulk moduli of 84.3 ± 14.8 and 77.7 ± 17.2 GPa using Voigt and Reuss averages, respectively. Both values are in good agreement with experimentally determined values of 82.9 ± 1.4 GPa[33] and the estimate based on fits to the Birch-Murnaghan equation of state.[20]

IV. PHENOMENOLOGICAL GINZBURG-LANDAU MODEL

To aid the interpretation of the *ab initio* results, we develop a phenomenological magneto-elastic Ginzburg-Landau model to capture the physics of the simultaneous sign-changing jump of the orthorhombicity and reversal of the AFM and FM directions. As pointed out by Refs. 9, 11 and 35, the magnetic structure of the iron pnictides consists of two interpenetrating Néel sublattices, with magnetizations $\mathbf{M}_1$ and $\mathbf{M}_2$ of equal amplitude that can point either parallel or antiparallel to each other (see Fig. 6).
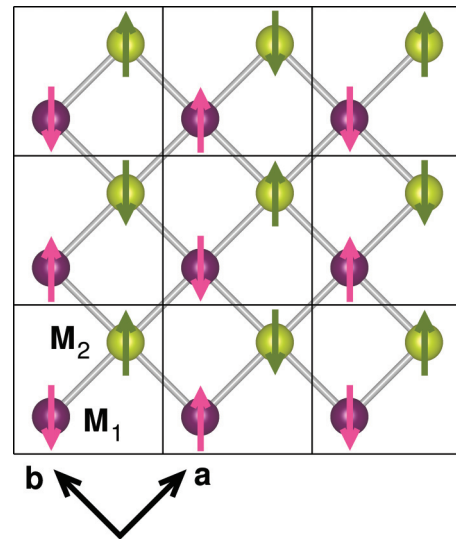

FIG. 6. (Color online) Magnetic structure of the iron pnictides consisting of two interpenetrating Néel sublattices, with magnetizations $\mathbf{M}_1$ and $\mathbf{M}_2$.

By including also the orthorhombic order parameter $\delta = (a - b)/(a + b)$, we obtain the Ginzburg-Landau free energy,

$$F = \frac{a_m}{4}\left(M_1^2 + M_2^2\right) + \frac{u_m}{16}\left(M_1^2 + M_2^2\right)^2 - \frac{g_m}{4}(\mathbf{M}_1 \cdot \mathbf{M}_2)^2$$
$$+ \frac{a_s}{2}\delta^2 + \frac{u_s}{4}\delta^4 + \frac{\lambda}{2}\delta(\mathbf{M}_1 \cdot \mathbf{M}_2) + \sigma\delta. \quad (3)$$

Here, $a_m \propto T - T_N$, $a_s \propto T - T_s$, $u_m, u_s > 0$, and $g_m > 0$. The last condition ensures that the ground state is the striped magnetic configuration (i.e., collinear $\mathbf{M}_1$ and $\mathbf{M}_2$). We also must have $u_m > g_m$ in order for the magnetic free energy to be bounded. $\lambda > 0$ is the magneto-elastic coupling and σ is the stress field conjugate to the orthorhombic order parameter. The sign of λ is set to describe the experimental observation that ferromagnetic bonds are shorter than antiferromagnetic bonds. Although this model does not take into account the physics of the magnetically driven structural transition, which comes from fluctuations beyond the Ginzburg-Landau analysis we perform below,[11] it captures the main features of the *ab initio* results.

The magnetic ground state is completely determined by the magnitude $M = |\mathbf{M}_1| = |\mathbf{M}_2|$ and the relative angle θ between $\mathbf{M}_1$ and $\mathbf{M}_2$. Then, minimization of the free energy leads to three coupled equations for M, θ, and δ:

$$\frac{\partial F}{\partial M} = (a_m + \lambda\delta\cos\theta)M + (u_m - g_m\cos^2\theta)M^3 = 0, \quad (4)$$

$$\frac{\partial F}{\partial \delta} = a_s\delta + u_s\delta^3 + \frac{\lambda}{2}M^2\cos\theta + \sigma = 0, \quad (5)$$

$$\frac{\partial F}{\partial \theta} = \frac{g_m}{4}M^4\sin 2\theta - \frac{\lambda}{2}M^2\delta\sin\theta = 0. \quad (6)$$

The last equation allows three possible solutions: $\theta = 0$, $\theta = \pi$, and $\cos\theta = \lambda\delta/(g_m M^2)$. We focus only on the $\theta = 0, \pi$ solutions, since they are the energy minimum at zero stress. In the ordered phase, where $a_m, a_s < 0$, we obtain the self-consistent equation for δ:

$$-\left(|a_s| + \frac{\lambda^2}{2(u_m - g_m)}\right)\delta + u_s\delta^3 = -\frac{\lambda|a_m|\cos\theta}{2(u_m - g_m)} - \sigma \quad (7)$$

For $\sigma = 0$, the mean-field equations and the free energy are invariant upon changing $\delta \to -\delta$ and $\theta \to \theta + \pi$. Thus, we have two degenerate solutions: $\delta > 0$ and antiparallel $\mathbf{M}_1$ and $\mathbf{M}_2$, $\theta = \pi$ (denoted hereafter δ_+), or $\delta < 0$ and parallel $\mathbf{M}_1$ and $\mathbf{M}_2$, $\theta = 0$ (denoted hereafter δ_-). The presence of a finite strain σ lifts this degeneracy. After defining

$$\delta_0 = \sqrt{\frac{|a_s|}{u_s} + \frac{\lambda^2}{2u_s(u_m - g_m)}},$$
$$h_+ = \frac{1}{u_s\delta_0^3}\left(\frac{\lambda|a_m|}{2(u_m - g_m)} - \sigma\right), \quad (8)$$
$$h_- = \frac{1}{u_s\delta_0^3}\left(\frac{\lambda|a_m|}{2(u_m - g_m)} + \sigma\right),$$

the self-consistent equations for the two solutions δ_+ and δ_- become simply

$$-\left(\frac{\delta_\pm}{\delta_0}\right) + \left(\frac{\delta_\pm}{\delta_0}\right)^3 = \pm h_\pm, \quad (9)$$

and we obtain analytic expressions for the two possible solutions:

$$\delta_\pm(h_\pm) = \pm\delta_0\left[\left(\frac{h_\pm}{2} + \sqrt{\frac{h_\pm^2}{4} - \frac{1}{27}}\right)^{\frac{1}{3}}\right.$$
$$\left. + \left(\frac{h_\pm}{2} - \sqrt{\frac{h_\pm^2}{4} - \frac{1}{27}}\right)^{\frac{1}{3}}\right]. \quad (10)$$

The interplay between the external stress field σ and the magneto-elastic coupling λ becomes evident in Eqs. (8)–(10). For $\sigma = 0$, λ acts as an external field of the same magnitude for both the δ_+ and δ_- solutions, i.e., it gives rise to nonzero $h_+ = h_-$ in the equations of state (9), making these two solutions degenerate. Now, consider that for $\sigma = 0$ the system chooses the minimum δ_+ (i.e., $\delta > 0$ and $\theta = \pi$). By increasing the external stress to a small value $\sigma > 0$, the effective field h_+ is suppressed, whereas the field h_- is enhanced. Although the solution δ_- (i.e., $\delta < 0$ and $\theta = 0$) has a lower energy, the solution δ_+ is still a local minimum, since the effective field h_+ is still finite. This situation persists until σ increases to the point where the field h_+ becomes negative and large enough to make the δ_+ solution not a local minimum.

In particular, to determine when the δ_+ solution ceases to be a local minimum, we analyze when one of the eigenvalues of the Hessian matrix ($\partial^2 F/\partial q_i \partial q_j$) becomes negative (with generalized coordinates $q_i = M, \delta, \theta$). The three eigenvalues μ_i are given by

$$\mu_\pm = \frac{1}{2}[a_s + 3u_s\delta^2 + 2M^2(u_m - g_m)]$$
$$\pm \frac{1}{2}\sqrt{[a_s + 3u_s\delta^2 - 2M^2(u_m - g_m)]^2 + 4\lambda^2 M^2},$$
$$\mu_0 = \frac{M^2}{2}(g_m M^2 - \lambda\delta\cos\theta). \quad (11)$$

For the δ_+ ($\delta > 0$, $\theta = \pi$) solution, the only eigenvalue that can become negative with increasing σ is μ_-. We find that this happens when the condition $\frac{\delta_+}{\delta_0} = -\frac{3}{2}h_+$ is met, corresponding to an effective field $h_+ = -\frac{2}{3\sqrt{3}}$, i.e., to the critical stress

$$\sigma_c = \frac{\lambda|a_m|}{2(u_m - g_m)} + \frac{2u_s}{3\sqrt{3}}\left(\frac{|a_s|}{u_s} + \frac{\lambda^2}{2u_s(u_m - g_m)}\right)^{3/2}. \quad (12)$$

At $\sigma = \sigma_c$, the solution $\delta > 0$, $\theta = \pi$ is not a local minimum any longer and the system jumps to the new minimum with $\delta < 0$, $\theta = 0$, where not only the sign of the orthorhombicity is reversed, but also the angle between the magnetizations of the two sublattices (i.e., the AFM and FM directions). This behavior is shown in Fig. 7 for a particular set of parameters.

To compare with the DFT results, we performed a slight modification with respect to the calculations presented in the previous section. To ensure that the external stress couples mainly to the orthorhombic mode δ and not to the longitudinal elastic mode ϵ, such that it does not change the volume of the system, we simultaneously applied positive (compressive) pressure along **a** and equal-amplitude negative (tensile) pressure along **b**. By doing this, we avoid terms such as $M^2\epsilon$ in the free energy, rendering the comparison between the *ab initio* and the Ginzburg-Landau results more meaningful.
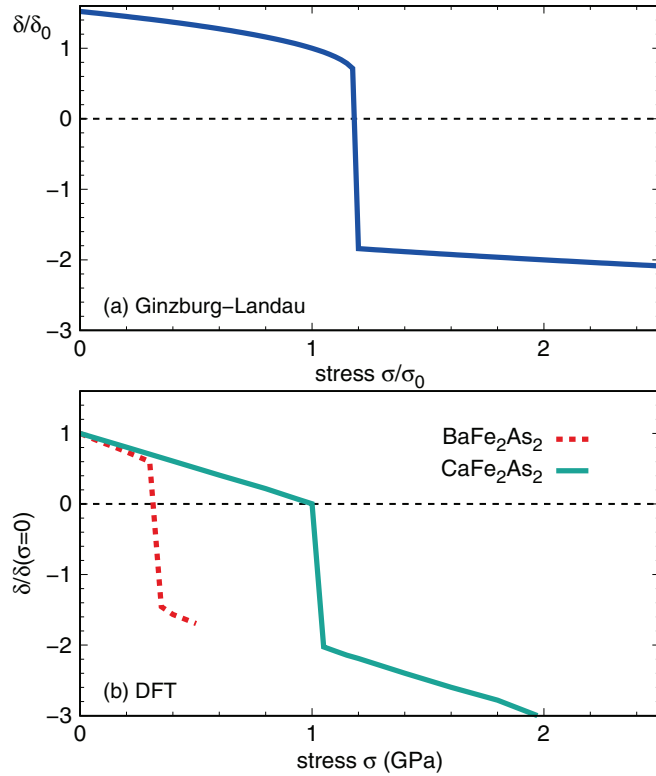
FIG. 7. (Color online) (a) Orthorhombic order parameter $\delta = \frac{a-b}{a+b}$ (in units of $\delta_0 = \sqrt{\frac{|a_s|}{u_s} + \frac{\lambda^2}{2u_s(u_m - g_m)}}$) as a function of the applied stress σ (in units of $\sigma_0 = \frac{\lambda |a_m|}{2(u_m - g_m)}$). We used parameters such that $\frac{\lambda |a_m|}{2(u_m - g_m)u_s \delta_0^3} = 2$. The jump happens when the $\delta > 0$ solution is no longer a local minimum, and is accompanied by a reversal of the angle between the two sublattice magnetizations $\mathbf{M}_1$ and $\mathbf{M}_2$, i.e., a reversal of the AFM and FM directions. (b) DFT results for the strain-dependent orthorhombic order parameter $\delta \equiv \frac{a-b}{a+b}$. The blue curve is for BaFe$_2$As$_2$ and the red curve, for CaFe$_2$As$_2$.

The *ab initio* obtained behavior of δ as a function of σ, defined in the way described above, is shown also in Fig. 7. We find a qualitative agreement with the Ginzburg-Landau results, showing that the external stress indeed competes with the magneto-elastic coupling, helping the system to overcome the energy barrier between the δ_+ ($\delta > 0$, $\theta = \pi$) and δ_- ($\delta < 0$, $\theta = 0$) solutions. A quantitative comparison becomes difficult because the DFT calculations are performed deep in the ordered phase, where higher order terms in the Ginzburg-Landau expansion become more important. Furthermore, it is also possible that some of the magnetic parameters (a_m, u_m, and g_m) have themselves some implicit pressure dependence in this regime. Nevertheless, we can use Eq. (12) as a benchmark to discuss differences in the BaFe$_2$As$_2$ and CaFe$_2$As$_2$ compounds. Clearly, Eq. (12) shows that σ_c increases with increasing magneto-elastic coupling. Therefore, the fact that σ_c is three times larger for CaFe$_2$As$_2$ than for BaFe$_2$As$_2$ suggests that, all other parameters being equal, the magneto-elastic coupling is larger in CaFe$_2$As$_2$ than in BaFe$_2$As$_2$. This may have important impact on the coupled magnetic and structural transitions displayed by these

compounds, as discussed in Refs. 11,35 and 36, and as such deserves further investigation in the future.

V. DISCUSSION AND CONCLUSIONS

In this paper, we analyzed the effects of tensile and compressive stress along **a**, **b**, and **a** + **b** on BaFe$_2$As$_2$ and CaFe$_2$As$_2$ by means of DFT calculations under constant stress conditions with the help of the FIRE algorithm, combined with a phenomenological Ginzburg-Landau model. Starting from the low-temperature magnetically ordered orthorhombic phase, we found in the pressure range between -2 and 2 GPa no real structural phase transitions in both systems except for a pronounced orthorhombicity jump accompanied by a 90 degree rotation of the magnetic order. FM and AFM directions are interchanged, as are the orbital occupations d_{xz} and d_{yz}. This inversion of axes is a direct consequence of the interplay between the intrinsic magneto-elastic coupling and the applied stress, as revealed by our Ginzburg-Landau analysis. The proportionality between the critical stress where this inversion happens and the value of the magneto-elastic coupling suggests that in CaFe$_2$As$_2$ the magnetic and structural degrees of freedom are more strongly coupled than in BaFe$_2$As$_2$, which may be related to the differences observed in their magnetic and structural transitions.[36] We also point out that the estimates for the bulk moduli of BaFe$_2$As$_2$ and CaFe$_2$As$_2$ derived from our *ab initio* results are in good agreement with the experimental measurements.

Our calculations also provide important insight on the impact of uniaxial stress on the magnetic properties of the pnictides. Figure 2 shows that the magnetic moment at zero temperature always decreases (increases) with compressive (tensile) stress, regardless of the axis that is perturbed. Unlike the jump in the orthorhombicity and the reversal of the FM and AFM directions, this is a consequence not of the magneto-elastic coupling, but of the changes in the pnictogen height promoted by the uniaxial stress. This is an important prediction of our first-principle calculations that can be tested experimentally. Interestingly, recent neutron diffraction experiments[6] on BaFe$_2$As$_2$ observed that upon application of compressive stress along the **b** axis, the magnetic moment is suppressed from $1.04\mu_B$ to $0.87\mu_B$. Given the small values of applied pressure, it could be that this suppression is due to a reduction of the volume fraction of the domains whose moments are oriented out of the scattering plane, as pointed out by the authors of Ref. 6. Nevertheless, in view of our current results, it would be interesting to either apply higher pressures to completely detwin the samples at low temperatures or to apply tensile stress to make a comparison with the case of compressive stress. We note that Ref. 6 also found an enhancement of the magnetic transition temperature T_N in the same detwinned samples. Phenomenological models[14,35,37] attribute this effect to changes in the magnetic fluctuation spectrum of the paramagnetic phase promoted by the uniaxial stress. In this regard, it would be interesting in future *ab initio* studies to systematically investigate the changes in the nesting feature of the Fermi surface (Fig. 3) as function of the uniaxial stress—specifically, changes in the (π,π) susceptibility peak.

Finally, we comment on the impact of our results to the understanding of the detwinning mechanism of iron

pnictide compounds. In the tetragonal phase, rather small uniaxial stress $P < 10$ MPa is enough to completely detwin the sample, giving rise to a single domain.[6,8,13] This can be understood as fluctuations above the structural transition temperature giving rise to long-range order in the presence of a symmetry-breaking field.[11] The situation is however very different deep in the orthorhombic phase, where twin domains are already formed. Experimentally, it is known that larger pressures are necessary to completely detwin the system in this case,[8,13] although specific values have not been reported, to our knowledge. One possible detwinning mechanism is the reversal of the orthorhombicity of one domain type, while the domain walls remain pinned. This corresponds precisely to the situation studied here, where the orthorhombicity jumps at a certain critical uniaxial pressure. Our *ab initio* results show that such a critical pressure for $BaFe_2As_2$ would be around 200 MPa—one order of magnitude larger than the pressure values necessary to detwin the sample in the tetragonal phase.

Of course, other mechanisms can also give rise to detwinning in the ordered phase, such as domain wall motion. Therefore, we propose controlled detwinning experiments at low temperatures in $BaFe_2As_2$ to measure the critical pressure necessary to form a single domain. Values comparable to the ones discussed here would be a strong indication for reversal of the order parameter inside fixed domains. Which mechanism is at play in the iron pnictides may have important consequences for the understanding of the impact of the external stress on the anisotropic properties measured in detwinned samples—particularly the in-plane resistivity anisotropy,[7,8,11] which is likely affected by domain wall scattering.[38]

APPENDIX: MODIFICATION OF THE FIRE ALGORITHM

Within the FIRE[19] algorithm, the energy minimization is achieved by moving the system's position r according to the following equation of motion:

$$\dot{v}(t) = \frac{F(t)}{m} - \gamma(t)|v(t)| \left[e_{v(t)} - e_{F(t)} \right], \quad (A1)$$

where e_x denotes the unit vector along x, with $x = v(t), F(t)$, t is time, and $\gamma(t)$ is a time-dependent friction parameter which assures that the system is moving down the energy hypersurface in an optimal manner as long as the power $P(t) = F(t) \cdot v(t)$ is positive. If $P(t)$ becomes negative, the procedure is stopped and relaxation is reinitialized in the direction of the steepest descent.

In order to use FIRE for the relaxation of periodic systems, we change from the configuration space of $3N$ atomic Cartesian coordinates r^α, $\alpha = 1, \ldots, N$, to an extended system of $3N + 9$ coordinates $\tilde{r}^\alpha = (s^\alpha, \hat{h})$, consisting of lattice vectors which are contained in columns of the 3×3 matrix $\hat{h} = (h_{ij})$, and fractional atomic positions s^α within the unit cell, where Cartesian and fractional positions are related by $r^\alpha = \hat{h}s^\alpha$.

When (A1) is rewritten in terms of coordinates $\tilde{r}^\alpha$, one just needs to find the appropriate expression for forces $\tilde{F}^\alpha$, that is, derivatives of energy with respect to the coordinates $\tilde{r}^\alpha$. Since stress and strain tensors, $\hat{\sigma}$ and $\hat{u}$, can be defined through

$$\hat{\sigma} = -\frac{1}{V}\frac{\partial E}{\partial \hat{u}}, \quad \hat{H} = (\hat{I} + \hat{u})\hat{h},$$

where $\hat{I}$ is the identity matrix and $\hat{H}$ is the lattice matrix after an infinitesimal deformation, it is easy to show that

$$\frac{\partial E}{\partial s^\alpha} = \sum_\beta \frac{\partial E}{\partial r^\beta}\frac{\partial r^\beta}{\partial s^\alpha} = \frac{\partial E}{\partial r^\alpha}\hat{h}^T = F^\alpha \hat{h}^T,$$

$$\frac{\partial E}{\partial \hat{h}} = \frac{\partial E}{\partial \hat{u}}\frac{\partial \hat{u}}{\partial \hat{h}} = \frac{\partial E}{\partial \hat{u}}(\hat{h}^T)^{-1} = -V\hat{\sigma}(\hat{h}^T)^{-1}, \quad (A2)$$

so that forces in the extended coordinates are given by

$$\tilde{F}^\alpha = [F^\alpha \hat{h}^T, \, -V\hat{\sigma}(\hat{h}^T)^{-1}]. \quad (A3)$$

Forces F^α and stresses $\hat{\sigma}$ are obtained from the electronic structure code, and are inserted directly into Eq. (A3), taking into account that $\hat{\sigma} = \hat{\sigma}^{\text{ext}} - \hat{\sigma}^{\text{int}}$, that is, total stress is the sum of internal and external stresses applied to the surface of the unit cell.

[1]Y. Kamihara, T. Watanabe, M. Hirano, and H. Hosono, J. Am. Chem. Soc. **130**, 3296 (2008).

[2]J. H. Chu, J. G. Analytis, K. De Greeve, P. L. McMahon, Z. Islam, Y. Yamamoto, and I. R. Fisher, Science **329**, 824 (2010).

[3]M. A. Tanatar, E. C. Bloomberg, A. Kreyssig, M. G. Kim, N. Ni, A. Thaler, S. L. Bud'ko, P. C. Canfield, A. I. Goldman, I. I. Mazin, and R. Prozorov, Phys. Rev. B **81**, 184508 (2010).

[4]H.-H. Kuo, J. H. Chu, S. C. Riggs, L. Yu, P. L. MacMahon, K. De Greeve, Y. Yamamoto, J. G. Analytis, and I. R. Fisher, Phys. Rev. B **84**, 054540 (2011).

[5]T. Liang, M. Nakajima, K. Kihou, Y. Tomioka, T. Ito, C. H. Lee, H. Kito, A. Iyo, H. Eisaki, T. Kakeshita, and S. Uchida, J. Phys. Chem. Solids **72**, 418 (2011).

[6]C. Dhital, Z. Yamani, W. Tian, J. Zeretsky, A. S. Sefat, Z. Wang, R. J. Birgeneau, and S. D. Wilson, Phys. Rev. Lett. **108**, 087001 (2012).

[7]E. C. Blomberg, A. Kreyssig, M. A. Tanatar, R. M. Fernandes, M. G. Kim, A. Thaler, J. Schmalian, S. L. Bud'ko, P. C. Canfield, A. I. Goldman, and R. Prozorov, Phys. Rev. B **85**, 144509 (2012).

[8]J.-H. Chu, H.-H. Kuo, J. G. Analytis, and I. R. Fisher, Science **337**, 710 (2012).

[9]C. Fang, H. Yao, W.-F. Tsai, J. Hu, and S. A. Kivelson, Phys. Rev. B **77**, 224509 (2008).

[10]C. Xu, M. Müller, and S. Sachdev, Phys. Rev. B **78**, 020501(R) (2008).

[11] R. M. Fernandes, L. H. VanBebber, S. Bhattacharya, P. Chandra, V. Keppens, D. Mandrus, M. A. McGuire, B. C. Sales, A. S. Sefat, and J. Schmalian, Phys. Rev. Lett. **105**, 157003 (2010).

[12] R. M. Fernandes, E. Abrahams, and J. Schmalian, Phys. Rev. Lett. **107**, 217002 (2011).

[13] E. C. Blomberg, M. A. Tanatar, A. Kreyssig, N. Ni, A. Thaler, R. Hu, S. L. Bud'ko, P. C. Canfield, A. I. Goldman, and R. Prozorov, Phys. Rev. B **83**, 134505 (2011).

[14] H. H. Kuo, J. G. Analytis, J.-H. Chu, R. M. Fernandes, J. Schmalian, and I. R. Fisher, Phys. Rev. B **86**, 134507 (2012).

[15] Q. Y. Wang, Z. Li, W. H. Zhang, Z. C. Zhang, J. S. Zhang, W. Li, H. Ding, Y. B. Ou, P. Deng, K. Chang, J. Wen, C. L. Song, K. He, J. F. Jia, S. H. Ji, Y. Wang, L. Wang, X. Chen, X. Ma, and Q. K. Xue, Chin. Phys. Lett. **29**, 037402 (2012).

[16] A. Cano and I. Paul, Phys. Rev. B **85**, 155133 (2012).

[17] G. Kresse and J. Hafner, Phys. Rev. B **47**, 558 (1993); G. Kresse and J. Furthmüller, *ibid*. **54**, 11169 (1996); Comput. Mater. Sci. **6**, 15 (1996).

[18] P. E. Blöchl, Phys. Rev. B **50**, 17953 (1994); G. Kresse and D. Joubert, *ibid*. **59**, 1758 (1999).

[19] E. Bitzek, P. Koskinen, F. Gähler, M. Moseler, and P. Gumbsch, Phys. Rev. Lett. **97**, 170201 (2006).

[20] M. Tomić, R. Valentí, and H. O. Jeschke, Phys. Rev. B **85**, 094105 (2012).

[21] Y.-Z. Zhang, H. C. Kandpal, I. Opahle, H. O. Jeschke, and R. Valentí, Phys. Rev. B **80**, 094530 (2009).

[22] N. Colonna, G. Profeta, A. Continenza, and S. Massidda, Phys. Rev. B **83**, 094529 (2011).

[23] N. Colonna, G. Profeta, and A. Continenza, Phys. Rev. B **83**, 224526 (2011).

[24] M. Aichhorn, L. Pourovskii, V. Vildosola, M. Ferrero, O. Parcollet, T. Miyake, A. Georges, and S. Biermann, Phys. Rev. B **80**, 085101 (2009).

[25] Z. P. Yin, K. Haule, and G. Kotliar, Nat. Mater. **10**, 932 (2011).

[26] M. Aichhorn, L. Pourovskii, and A. Georges, Phys. Rev. B **84**, 054529 (2011).

[27] J. Ferber, K. Foyevtsova, R. Valentí, and H. O. Jeschke, Phys. Rev. B **85**, 094505 (2012).

[28] J. Ferber, H. O. Jeschke, and R. Valentí, Phys. Rev. Lett. **109**, 236403 (2012).

[29] P. Werner, M. Casula, T. Miyake, F. Aryasetiawan, A. J. Millis, and S. Biermann, Nat. Phys. **8**, 331 (2012).

[30] A. Kreyssig, M. A. Green, Y. Lee, G. D. Samolyuk, P. Zajdel, J. W. Lynn, S. L. Bud'ko, M. S. Torikachvili, N. Ni, S. Nandi, J. B. Leão, S. J. Poulton, D. N. Argyriou, B. N. Harmon, and R. J. McQueeney, Phys. Rev. B **78**, 184517 (2008).

[31] J. D. Clayton, *Nonlinear Mechanics of Crystals* (Springer, New York, 2010).

[32] J. E. Jörgensen and T. C. Hansen, Eur. Phys. J. B **78**, 411 (2010).

[33] R. Mittal, S. K. Mishra, S. L. Chaplot, S. V. Ovsyannikov, E. Greenberg, D. M. Trots, L. Dubrovinsky, Y. Su, Th. Brueckel, S. Matsuishi, H. Hosono, and G. Garbarino, Phys. Rev. B **83**, 054503 (2011).

[34] O. K. Andersen and L. Boeri, Ann. Phys. (NY) **523**, 8 (2011).

[35] A. Cano, M. Civelli, I. Eremin, and I. Paul, Phys. Rev. B **82**, 020408(R) (2010).

[36] V. Barzykin and L. P. Gor'kov, Phys. Rev. B **79**, 134510 (2009).

[37] J. Hu, C. Setty, and S. Kivelson, Phys. Rev. B **85**, 100507(R) (2012).

[38] I. I. Mazin and M. D. Johannes, Nat. Phys. **5**, 141 (2009).